

Soft spots of net negative topological charge directly cause the plasticity of 3D glasses

Arabinda Bera¹, Matteo Baggioli^{2,*}, Timothy C. Petersen³, Amelia C. Y. Liu^{5,†} and Alessio Zaccone^{1,‡}

¹*Department of Physics “A. Pontremoli”, University of Milan, via Celoria 16, 20133 Milan, Italy*

²*Wilczek Quantum Center, School of Physics and Astronomy, Shanghai Jiao Tong University, Shanghai 200240, China*

³*Monash Centre for Electron Microscopy, Monash University, Clayton, 3800, Victoria, Australia & School of Physics and Astronomy, Monash University, Clayton, 3800, Victoria, Australia*

⁴*US DEVCOM Army Research Laboratory, Maryland, United States and*

⁵*School of Physics and Astronomy, Monash University, Clayton, 3800, Victoria, Australia*

The deformation mechanism in amorphous solids subjected to external shear remains poorly understood because of the absence of well-defined topological defects mediating the plastic deformation. The notion of soft spots has emerged as a useful tool to characterize the onset of irreversible rearrangements and plastic flow, but these entities are not well-defined in terms of geometry and topology. In this study, we unveil the phenomenology of recently discovered, well-defined topological defects governing the microscopic mechanical and yielding behavior of a model 3D glass under shear deformation. We identify the existence of vortex-like and anti-vortex-like topological defects within the 3D non-affine displacement field. The number density of these defects exhibits a significant (inverse) correlation with the plastic events, with defect proliferation-annihilation cycles matching the alternation of elastic-like segments and catastrophic plastic drops, respectively. Furthermore, we observe collective annihilation of these point-like defects via plastic events, with large local topological charge fluctuations in the vicinity of regions that feature strong non-affine displacements. We unveil that plastic yielding is driven by very few, but very large, clusters of net negative topological charge, the massive annihilation of which triggers the onset of plastic flow. These findings suggest a geometric and topological characterization of soft spots and pave the way for the mechanistic understanding of topological defects as mediators of plastic deformation in glassy materials.

Introduction – While plastic deformations in crystals are by now well understood in terms of dislocation dynamics, a concept originally proposed by Taylor [1], identifying the physical mechanism of plasticity in amorphous solids, such as glasses, is more challenging [2]. Despite several attempts to generalize the concept of topological defects and dislocation-like structures in amorphous solids [3–6], not much progress in this direction has been achieved so far, and this approach is still considered by many as hopeless, due to the unavoidable disordered reference structure [7]. Other existing viewpoints on this matter, such as shear transformation zone (STZ) theory [8], 2D melting-type scenarios [9] or elastoplastic models [10], assume the existence of soft spots linked to some unspecified defects, but they are purely phenomenological and agnostic about the precise definition of the latter. In particular, soft spots, as discussed in the literature [11], lack a quantitative geometric characterization or measure to identify them, in contrast to topological defects in crystalline matter and liquid crystals [12]. At the same time, novel ideas to identify defects in amorphous solids based on quasi-localized modes [13], geometric charges [14] or string-like defects [15, 16] are not mature enough; consequently, structural indicators [17] remain still the best available option to predict plasticity in glasses.

Recently, substantial progress has been achieved by looking for defects beyond the paradigm of the static structure. Following this idea, well-defined topological

defects have been discovered in the shear deformation of simulated polymer glasses [18]. These defects were identified with singularities in the displacement field, which emerge in the non-affine part \mathbf{u} of the total displacement field $\mathbf{u}_t = \mathbf{u}_A + \mathbf{u}$, where \mathbf{u}_A is the smooth affine contribution [19–21]. As for dislocations in ordered crystals [22], a circulation integral around such topological defects connects to the incompatibility of the strain field, *i.e.* the curl of the curl of the strain tensor does not vanish. This is, in turn, mathematically equivalent to a Bianchi identity for the displacement field which is violated topologically due to the presence of a finite Burgers vector, and to the explicit breaking of an emergent higher-form symmetry [23].

Shortly thereafter, further evidence of the existence of well-defined topological defects in glasses came from the analysis of eigenvectors in 2D simulated glasses [24, 25]. It was found that, even without applying any deformation to the 2D glass, a circulation integral of the angle between the y and x components of the eigenvectors of the Hessian matrix yields vortex-like defects with quantized +1 charge, and anti-vortex-like defects with quantized -1 charge. Moreover, spatial correlation between the negative topological charges and the soft regions most inclined to plastic deformation was found. Interestingly, the dynamics of vortex-like defects in the displacement field have been already connected in the past to the formation of shear transformation zones [26, 27], confirming

their importance for the description of plasticity in amorphous solids.

Almost at the same time with the current paper, a preprint [28] has been posted, where the concept of topological defects has been used to unambiguously identify shear transformation zones in 2D amorphous solids, providing a direct connection between individual topological defects with negative charge and local structural rearrangements responsible for plasticity.

In this study, we establish a protocol for identifying quantized (± 1) topological defects in the displacement field of model 3D glasses undergoing shear deformation. Through defect analysis of diverse 2D slices within the shear plane, we demonstrate a correlation between the population of topological defects and plastic drops in stress-strain. Further dissection of these 2D slices reveals microscopic details on local topological charge and associated non-affinity. Notably, fluctuations in topological charge are observed in proximity to regions exhibiting strong non-affine displacements, indicating the emergence of soft spots. Systematic analysis of various 2D slices enables the construction of a three-dimensional representation of topological charges originating from point defects, highlighting the drastic annihilation of such defects during yielding – a “topological catastrophe”.

Results – Here we prepare a polymer glass sample at $T = 0$ implemented using the Kremer-Grest model [29]. The system is then subjected to an athermal quasi-static (AQS) shearing protocol involving affine transformation by small strain increments of $\delta\gamma_{xz} = 0.001$ in the xz plane following energy minimization. More details on the interaction potential and the deformation protocol of the simulations are provided in the method section.

During the deformation, we determine the total displacement field \mathbf{u}_t by taking the difference between two successive snapshots separated by $\delta\gamma_{xz} = 0.001$. The affine displacement field here is calculated as $\mathbf{u}_A = \delta\gamma_{xz} z_{\text{eff}} \hat{x}$, where z_{eff} represents the effective distance from the base of the box along the z -direction.

The non-affine field is defined as $\mathbf{u} = \mathbf{u}_t - \mathbf{u}_A$ [21], and can be expressed as $\mathbf{u} = \mathbf{u}_{\parallel} + \mathbf{u}_{\perp}$, where \mathbf{u}_{\parallel} is the vector in the xz (shear) plane, and \mathbf{u}_{\perp} is the vector along the y -direction. The average magnitude of non-affine displacement in three dimensions is computed as $u_{\text{mag}}^{3D} = \frac{1}{N} \sum_{i=1}^N |\mathbf{u}_i|$. As the shear is applied along the x -direction to deform the xz (shear) plane, we compute the average non-affine displacement in the xz plane as $u_{\text{mag}} = \langle \frac{1}{N_s} \sum_{i=1}^{N_s} |\mathbf{u}_{\parallel,i}| \rangle$, where $\langle \dots \rangle$ denotes the average over all slices along the y direction, and N_s represents the number of particles in each two-dimensional (2D) slice. For our analysis, we divided the 3D box into numerous two-dimensional slices of width 2σ (σ is the monomer diameter) along the y direction.

In Fig.1, we present the stress (σ) versus strain (γ) curve. Additionally, we plot the average magnitudes of

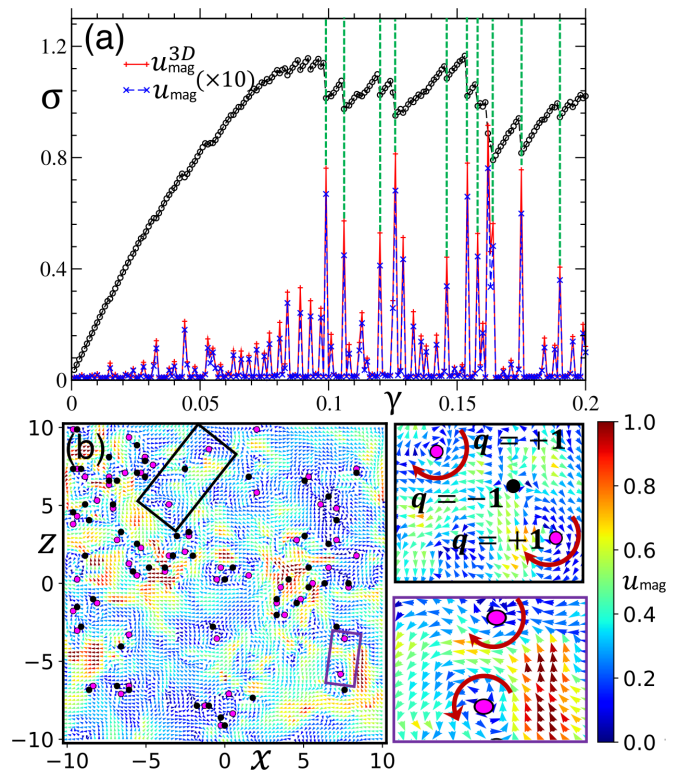


FIG. 1: **(a)** The stress versus strain curve is plotted, accompanied by red lines representing the average magnitudes of non-affine displacement in three dimensions (u_{mag}^{3D}) and blue lines illustrating the average magnitude of the non-affine field in the xz plane (u_{mag}). The green dashed lines are indicative of the “major plastic events”. **(b)** Normalized non-affine displacement field presented for a 2D slice within the xz plane at $y = 0$, with $\gamma = 0.098$. Circles filled in magenta and black represent topological defects with winding numbers $q = +1$ and -1 , respectively. Enlarged views of specific regions (outlined by the rectangular boxes) emphasize the chirality of the defects (described by the red arcs). The color bar illustrates the magnitude of non-affine displacement.

the non-affine displacement, denoted as u_{mag}^{3D} and u_{mag} , represented by red and blue lines, respectively. The stress drop is notably identifiable by the peaks in the non-affine displacement values. These peaks in u_{mag}^{3D} and u_{mag} are evidently commensurate with the occurrence of plastic events. We have highlighted several of these plastic events using green dashed lines in Fig.1. Remarkably, we observe that u_{mag} , which disregards the y -component of the field, can accurately identify the locations of plastic events. This observation implies that the characteristics of displacement field remain consistent when we exclude the y -component (orthogonal to the shear plane).

We investigate point-like topological defects by analyzing the non-affine displacement fields within various 2D slices orthogonal to the y direction. We construct circulation integrals along closed loops \mathcal{L} and calculate the

winding number q as:

$$q = \frac{1}{2\pi} \oint_{\mathcal{L}} d\theta = \frac{1}{2\pi} \oint_{\mathcal{L}} \vec{\nabla}\theta \cdot d\vec{\ell}, \quad (1)$$

where θ represents the phase angle of the non-affine field, defined as $\theta = \arctan(u^z/u^x)$ with reference to the Cartesian z and x components of the non-affine displacement field in the shear plane. Furthermore, $d\vec{\ell}$ denotes the line elements along the closed loop \mathcal{L} . The winding number $q \in \mathbb{Z}$ is referred to as the topological charge.

In 2D, a point defect carrying a winding number of $q = +1$ is recognized as a vortex, while a defect with $q = -1$ is identified as an anti-vortex. We systematically discerned these point defects across various 2D slices within the xz plane. As depicted in Fig.1(b), we present the interpolated non-affine displacement field with a color bar indicating the scaled magnitude, within a 2D slice at $y = 0$ for $\gamma = 0.098$. The existence of topological defects with winding numbers $q = +1$ and $q = -1$ is marked by magenta and black-filled circles, respectively. Notably, two rectangular regions are selectively magnified to elucidate the chirality of vortices ($q = +1$). At the frustrated interface between two vortices of identical phase chirality (direction of swirls), an anti-vortex ($q = -1$) is observed. Conversely, vortices with opposing phase chiralities exhibit a stable interface, as portrayed in the enlarged sections of Fig. 1(b). This intriguing pattern bears resemblance to topological defects discerned in the eigenvectors field of a recently investigated 2D glass [24]. As shown in [28], the displacement and stress distribution of -1 defects strongly resemble those of an Eshelby inclusion with quadrupolar structure, *i.e.* a shear transformation zone.

In Fig.2, we present the locations of point-defects within the xz plane non-affine displacement field at $y = 0$ for four consecutive γ values that straddle the yielding point. These snapshots reveal a significant transformation in the structure of defects. We compute the total number of these point defects in the non-affine displacement field across various xz planes by varying y and calculate the average number of defects N_d per slice. In order to establish a connection between plastic events and the emergence of point-like topological defects, we compute N_d with increasing strain γ .

In Fig.3(a), we illustrate the relative changes in the average magnitude of the displacement field (u_{mag}) and the average number of defects (N_d) per slice within a range of γ . It is notable that the peaks in u_{mag} correspond to dips in the total number of point defects. This observation strongly suggests an anti-correlation between u_{mag} and N_d , implying that accumulation of topological defects is the trigger of plastic events via subsequent defects annihilation.

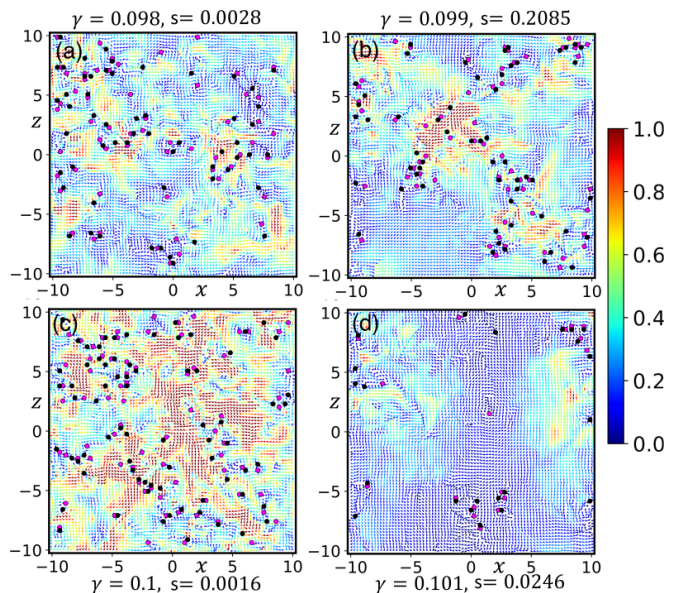


FIG. 2: (a)-(d) Normalized displacement field for four consecutive γ values within the 2D slice at $y = 0$. Topological defects are represented by circles filled by magenta ($q = +1$) and black ($q = -1$). The color bar (scaled by the factor s) indicates the magnitude of the displacement field. Note that the range of the displacements varies by two orders of magnitudes and the displacements are extremely large around yielding (panel (b)).

To explore this dependence further, we calculate the Pearson correlation coefficient (PCC) [30] as:

$$\text{PCC} = \frac{\sum_{\{\gamma\}} (u_{\text{mag}} - \bar{u}_{\text{mag}})(N_d - \bar{N}_d)}{\sqrt{\sum_{\{\gamma\}} (u_{\text{mag}} - \bar{u}_{\text{mag}})^2} \sqrt{\sum_{\{\gamma\}} (N_d - \bar{N}_d)^2}}, \quad (2)$$

where \bar{u}_{mag} and \bar{N}_d represent the average values of u_{mag} and N_d over the range of strain $\gamma \in [0, 0.2]$, respectively. The value of PCC falls within the range of $[-1, 1]$, where a value close to 1 indicates a strong positive correlation, while a value near -1 suggests a strong negative correlation. For the considered range of γ , we obtain the value of PCC ≈ -0.5 , indicating a marked level of anti-correlation. Interestingly, when we consider only the data points associated with plastic events, identified from the peaks of u_{mag} , the value of PCC approaches -1 . This suggests that there is a strong (inverse) relationship between the topological defects and plastic deformation events in the material.

While we have established a robust anti-correlation between plastic events and the variation in the total number of topological point defects, our primary objective is to understand the microscopic details of these plastic events and investigate the specific role played by the topological defects. Upon examining the snapshots in Figs.1(b) and 2, we observe that topological defects tend to be posi-

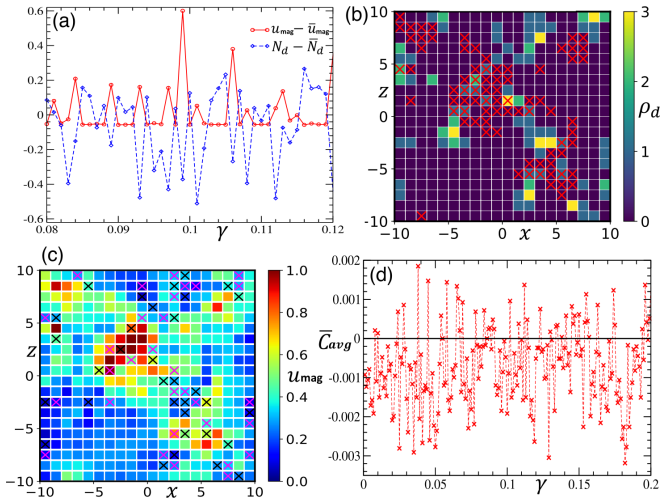


FIG. 3: **(a)** The magnitude of non-affine displacement field (u_{mag}) and the average defect number N_d are shown in certain range of γ values. Both quantities are presented after subtracting their respective average values, and the N_d values have been scaled by 0.01 for better visualization. **(b)** A 2D slice ($\gamma = 0.099$ and $y = 0$) dissected into many unit area square cells is shown with the local topological number density ρ_d in each cell by color bar. The cells having larger non-affine magnitude have been presented by red crosses. **(c)** The same slice, as in (b), shown by color (scaled by 0.2) which represents the local magnitude of non-affine displacement. The cells marked by crosses colored in magenta and black are populated by topological charges with positive and negative values, respectively. **(d)** The average topological charge density \bar{C}_{avg} per slice is shown with the variation of γ .

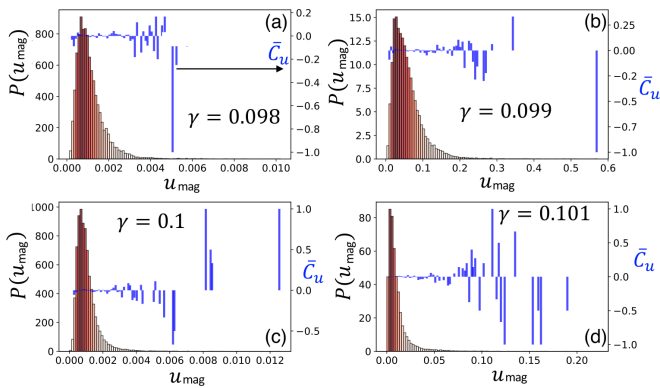


FIG. 4: **(a)-(d)** The distribution of u_{mag} and associated average topological charge \bar{C}_u per cell are shown for several γ values. Note that there is large variation in the magnitude of the displacements as a function of strain.

tioned in close proximity to regions characterized by high non-affine displacement magnitudes. In order to investigate whether the local non-affine displacement field correlates with the presence of topological defects, we systematically partition each 2D slice into numerous unit area square cells, as illustrated in Figs.3(b) and (c). Within each such cell, we compute the number density of defects

n_d , average non-affine displacement u_{mag} and concurrently measure the local topological charge in each cell, denoted as $\bar{C}_k = \sum_{j \in \mathcal{S}_k} q_j$, where q_j is the topological charge of defects present inside the k -th cell, \mathcal{S}_k . In fact, \bar{C}_k essentially measures the topological charge imbalance inside each cell. The average topological charge imbalance is computed as $\bar{C}_{\text{avg}} = (1/n_{\text{cell}}) \sum_{k=1}^{n_{\text{cell}}} \bar{C}_k$, where n_{cell} is the total number of square cells. Let us emphasize that this analysis probes a mesoscopic coarse-grained length scale corresponding to the size of the (square) sub-cell of length σ and does not reveal any local microscopic information.

In Fig.3(b) and (c), we visually illustrate the partitioning of a 2D slice into multiple square cells, utilizing a color bar to represent the number density of topological defects (n_d) and the magnitude of the non-affine displacement field (u_{mag} within each cell), respectively. The red crosses in Fig. 3(b) pinpoint cells where u_{mag} is notably higher compared to other cells, while colours of the crosses within several cells in Fig.3(c) demarcate the signs of the average topological charge, denoted as \bar{C}_{avg} . Magenta highlights cells with $\bar{C}_k \geq 1$, and black designates cells with $\bar{C}_k \leq -1$. In Fig.3(d), we present the average local topological charge imbalance \bar{C}_{avg} , computed across all cells and various 2D slices, while varying γ . Remarkably, we observe a prevailing bias in local charge imbalance towards net negative charge values, which we attribute as an underlying tendency towards plastic deformation.

In Fig.4(a)-(d), we further analyze the distribution of u_{mag} and the corresponding average topological charge imbalance \bar{C}_u across different u_{mag} values, where the average is performed over cells with same u_{mag} . We observe much greater fluctuations in local charge imbalance at higher non-affine displacements. The pronounced charge imbalance at higher non-affine field suggests the formation of mesoscopic soft spots possessing a net topological charge, upon approaching yielding.

To investigate the development of these soft spots, we calculate the distribution of u_{mag} for coarse-grained cells with local topological charge $\bar{C}_k > 1$ or $\bar{C}_k < -1$. In Fig. 5, we present this distribution for positive and negative charge imbalances towards the approach of two plastic events at $\gamma = 0.099$ and $\gamma = 0.154$. Notably, distinct peaks in these distributions at high u_{mag} are almost always associated with a net negative charge, showing how the negative defects clusters emerge as soft spots at the onset of yielding.

Our analysis has primarily focused on various 2D cross-sections within the xz plane along the y axis. In order to extend our observations into three dimensions, we developed a generalized protocol to systematically scan the system from arbitrary directions. Positions of topological

defects were identified across numerous two-dimensional slices, each oriented along a direction vector \hat{n} . By considering various directions \hat{n} uniformly distributed on a unit sphere, we located defects within the simulation box. Similar to the dissection of 2D slices illustrated in Fig. 3(b) and (c), we partitioned the entire simulation box into cubical cells of unit volume. Utilizing the locations of topological defect points identified from 2D dissections along all possible directions, we computed the local topological charge imbalance \bar{C}_k^c (scaled within the range [0,1]) within these cubical cells.

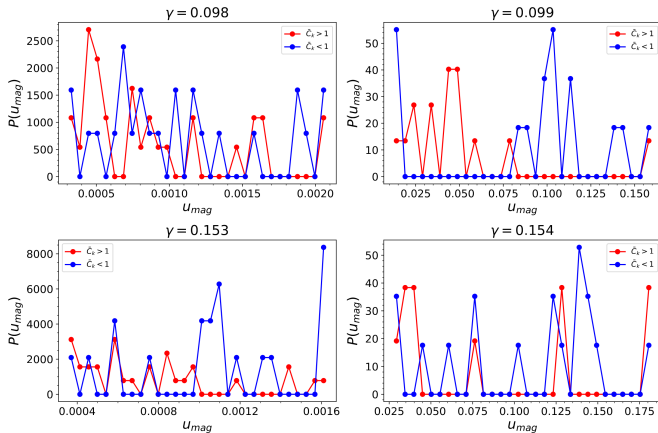


FIG. 5: (a)-(d) The normalised distribution function that measures the probability of obtaining topological charge $\bar{C}_k > 1$ and $\bar{C}_k < -1$ at different local regions having average non-affine displacement magnitude (u_{mag}) are shown at the vicinity of two major plastic events at $\gamma = 0.099$ and $\gamma = 0.154$.

We examine the spatial distribution and probability distribution of connected cells that had high net charge imbalance of the same sign. We then calculate the normalized cluster size distribution $P(n_c)$, where n_c represents the number of connected cubical cells with a high topological charge of the same sign. In Fig.6(a)-(d), we depict the cluster size distribution $P(n_c)$ for $\bar{C}_k^c > 0.6$ and $\bar{C}_k^c < -0.6$ during yielding. We have highlighted the three largest clusters in the distributions for $\gamma = 0.098$ and $\gamma = 0.099$ in Fig. 6(a)-(b). Right before yielding, we observe the emergence of very large clusters, with the largest one being of negative net charge imbalance. Right after yielding, these large clusters disappear and the distribution tends to narrow and fragment into clusters of smaller sizes. The rapid formation and disappearance of large clusters of negative topological charge – a “topological catastrophe” – suggests that yielding might be caused by the massive annihilation of topological defects. Furthermore, following the recent results presented in [28], the large clusters of negative topological charge, related to STZ, appearing before yielding might be a manifestation of the formation of shear bands. It is also plausible that the structure and dynamics of these defects bear strong connections with the concept of elastic screening

discussed in [14].

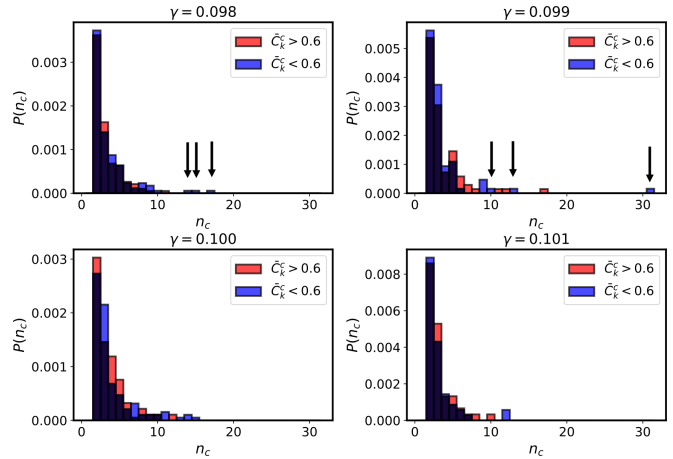


FIG. 6: (a)-(d) The normalised cluster size distribution $P(n_c)$ (n_c being the size of the cluster, *i.e.*, number of connected cubical cells) are plotted for positive and negative charges at different values of strain γ . Note that the overlapping regions between the distributions for positive and negative charges are plotted in black. The distributions have been normalised in such a way that the area under the curve is unity.

Conclusion – In this study, we systematically explored the formation, dynamics and statistical properties of topological defects in a 3D polymer glass model under shear deformation. We first established that, in 3D glasses, the topological defects with -1 charge (saddles or anti-vortices) are associated with large non-affine displacements and act as triggers of local plastic activity. Also, the total defects density anti-correlates with the non-affine displacements magnitude as a function of shear strain. This suggests that the transient accumulation of defects triggers a subsequent plastic event, upon further increasing the strain, via massive annihilation of negative and positive defects. Overall, the deformation process upon increasing the strain is characterized by a dominance of negative charges over positive charges, which is linked to the tendency of the polymer glass to strain-soften prior and across yielding. Through a coarse-graining procedure into mesoscopic cells, we unveiled the formation of very few, but very large, clusters bearing net negative topological charge right before the yielding point. These clusters are associated with huge values of the non-affine displacements magnitude. The emergence of these very large negative clusters right before yielding is followed by its massive annihilation right at yielding, which is accompanied by a system-spanning plastic event marking the onset of plastic flow.

Several open questions remain to be answered. As already anticipated in [28], topological defects with negative charge exhibit strong resemblances with quasi-localized quadrupolar fields previously identified as the carriers of plasticity in amorphous solids [31, 32].

Indeed, topological defects can be identified as geometric singularities even in amorphous systems [33, 34], and might constitute the building blocks for the dipolar and quadrupolar objects discussed in the literature in relation to elastic screening and anomalous elasticity [35]. These topological defects could provide the missing link to understand yielding in amorphous systems as a topological phase transition [34, 36], akin to the famous BKT transition in 2D crystals [9, 37].

Moreover, topological defects may provide a geometric definition for the liquid-like atomic environments [38] and display a strong connection with the emergence of unstable instantaneous modes, already associated in the literature to plastic instabilities [39, 40]. On the other hand, it would be interesting to analyze from a theoretical point of view how these topological defects manifest themselves within the tensor gauge theory for anomalous elasticity of [41, 42].

Finally, to give more credibility to this novel approach, it is imperative to identify these topological defects experimentally. Colloidal systems or granular matter systems seem to be the most promising playground for this scope. Microbeam x-ray scattering techniques, as used in [43], might also be able to detect the signatures of these topological defects. Finally, X-ray irradiation [44] could provide a method to induce and control the dynamics of the latter.

As a final remark, despite what has been thought for long time, topological concepts are still valid beyond the realm of structural order, and they emerge as the best candidates to characterize plasticity and mechanical failure in amorphous materials from a microscopic point of view, as achieved for the crystalline counterparts.

Methods – We use the Kremer-Grest model [29] to investigate a coarse-grained polymer system consisting of linear chains, each composed of 50 monomers. The monomer masses within a polymer chain alternate between two values, $m_1 = 1$ and $m_2 = 3$, with a total of $N = 10,000$ monomers in the system.

In our system, monomers interact through the potential:

$$U_{\text{LJ}}(r) = \begin{cases} u(r) - u(r_c), & \text{for } r < r_c = 2.5\sigma, \\ 0, & \text{otherwise.} \end{cases} \quad (3)$$

Here, $u(r)$ represents the standard Lennard-Jones (LJ) potential

$$u(r) = 4\varepsilon \left[\left(\frac{\sigma}{r} \right)^{12} - \left(\frac{\sigma}{r} \right)^6 \right], \quad (4)$$

where ε is the interaction strength, and σ is the diameter of each monomer. The inter-particle distance r is

constrained to be within the interaction range $r_c = 2.5\sigma$. Additionally, the covalent along-the-chain bonds are represented by a finite extensible nonlinear elastic (FENE) potential [29]:

$$U_{\text{FENE}}(r) = -\frac{Kr_0^2}{2} \ln \left[1 - \left(\frac{r}{r_0} \right)^2 \right]. \quad (5)$$

Here, we set the strength of the FENE interaction as $K = 30$ and the range $r_0 = 1.5\sigma$.

The polymer chains were placed within a three-dimensional cubic box and subjected to periodic boundary conditions in all directions. Equilibration of the system was conducted using the LAMMPS simulation package [45]. For the deformation process, we employed an athermal quasi-static (AQS) protocol utilizing the LAMMPS [45] environment. The glass sample is prepared at zero temperature and subsequently subjected to a quasi-static shear procedure with each strain step of $\delta\gamma_{xz} = 0.001$. We expressed mass, length, and time in units of m_1 , σ , and $\tau = (m_1\sigma^2/\varepsilon)^{1/2}$. In our study, we set m_1 , σ , and ε to unity. In all our simulations the chains are treated as fully-flexible, with no covalent-like bond-bending terms in the potential.

We systematically partitioned the simulation box into $20\sigma \times 20\sigma$ 2D slices of width 2σ along the xz -plane into a 80×80 square lattice. Subsequently, we executed an interpolation of non-affine displacement values at these lattice grid points. The interpolation has been performed using an in-built Python function “griddata” that takes as input the displacement field scattered data and gives the displacement field at each constructed lattice grid. At each grid point, the phase-angle θ of the non-affine field is determined. Utilizing nearest neighbor grid points, we systematically constructed closed square loops and compute the topological charge q at the central point of each such square loop using (1).

When approximating the contour integration with a discrete Riemann sum, precise numerical evaluation requires numerous points along the path or, equivalently, a small step between summation points. To isolate single defects in the plane, the circulation path can be contracted to the immediate vicinity, maintaining the topological index of the (potential) vortex core. Ensuring small steps between points is achieved by interpolating the smooth and continuous field near the suspected vortex core, preserving the topology. For efficient upscaling through interpolation, only a few points need sampling, as they are in close proximity. On a Cartesian grid, four points over a 2×2 pixel grid are numerically convenient. In clustered vortex scenarios, expanded circulation paths might inaccurately identify unresolved higher-order vortices (by encompassing multiple like-signed topological charges) or overlook vortices altogether (in the presence of an equal number of $-ve$ and $+ve$ signed vortices within the contour).

Acknowledgments – We would like to thank Y. Jin, D. Pan, W. Zhang, J. Zhang, M. Pica Ciamarra, M. Moshe and C. Jiang for useful discussions and collaboration on related topics. M.B. acknowledge the support of the Shanghai Municipal Science and Technology Major Project (Grant No.2019SHZDZX01). MB acknowledges the support of the sponsorship from the Yangyang Development Fund. ACYL acknowledges support from the Australian Research Council (FT180100594). A.Z. gratefully acknowledges funding from the European Union through Horizon Europe ERC Grant number: 101043968 “Multimech”, and from the Niedersächsische Akademie der Wissenschaften zu Göttingen in the frame of the Gauss Professorship program. A.Z. and A.B. gratefully acknowledge funding from US Army Research Office through contract nr. W911NF-22-2-0256.

* Electronic address: b.matteo@sjtu.edu.cn

† Electronic address: amelia.liu@monash.edu

‡ Electronic address: alessio.zaccone@unimi.it

- [1] G. I. Taylor, Proceedings of the Royal Society of London. Series A, Containing Papers of a Mathematical and Physical Character **145**, 362 (1934).
- [2] W. Wang, Y. Yang, T. Nieh, and C. Liu, *Intermetallics* **67**, 81 (2015).
- [3] J. J. Gilman, *Journal of Applied Physics* **44**, 675 (2003).
- [4] P. Chaudhari, A. Levi, and P. Steinhardt, *Phys. Rev. Lett.* **43**, 1517 (1979).
- [5] P. J. Steinhardt and P. Chaudhari, *Philosophical Magazine A* **44**, 1375 (1981).
- [6] T. Egami, K. Maeda, and V. Vitek, *Philosophical Magazine A* **41**, 883 (1980).
- [7] S. Alexander, *Physics Reports* **296**, 65 (1998).
- [8] M. L. Falk and J. S. Langer, *Phys. Rev. E* **57**, 7192 (1998).
- [9] D. Fraggedakis, M. R. Hasyim, and K. K. Mandadapu, *Proceedings of the National Academy of Sciences* **120**, e2209144120 (2023).
- [10] A. Nicolas, E. E. Ferrero, K. Martens, and J.-L. Barrat, *Rev. Mod. Phys.* **90**, 045006 (2018).
- [11] M. L. Manning and A. J. Liu, *Phys. Rev. Lett.* **107**, 108302 (2011).
- [12] S. Fumeron and B. Berche, *The European Physical Journal Special Topics* **232**, 1813 (2023).
- [13] E. Lerner and E. Bouchbinder, *The Journal of Chemical Physics* **155**, 200901 (2021).
- [14] A. Lemaitre, C. Mondal, M. Moshe, I. Procaccia, S. Roy, and K. Sreiber-Re'em, *Phys. Rev. E* **104**, 024904 (2021).
- [15] F. Lund, *Phys. Rev. B* **91**, 094102 (2015).
- [16] Z.-Y. Zhou, Y. Sun, L. Gao, Y.-J. Wang, and H.-B. Yu, *Acta Materialia* **246**, 118701 (2023).
- [17] D. Richard, M. Ozawa, S. Patinet, E. Stanifer, B. Shang, S. A. Ridout, B. Xu, G. Zhang, P. K. Morse, J.-L. Barrat, L. Berthier, M. L. Falk, P. Guan, A. J. Liu, K. Martens, S. Sastry, D. Vandembroucq, E. Lerner, and M. L. Manning, *Phys. Rev. Mater.* **4**, 113609 (2020).
- [18] M. Baggioli, I. Kriuchevskiy, T. W. Sirk, and A. Zaccone, *Phys. Rev. Lett.* **127**, 015501 (2021).
- [19] A. Tanguy, J. P. Wittmer, F. Leonforte, and J.-L. Barrat, *Phys. Rev. B* **66**, 174205 (2002).
- [20] B. A. DiDonna and T. C. Lubensky, *Phys. Rev. E* **72**, 066619 (2005).
- [21] A. Zaccone, *Theory of Disordered Solids* (Springer, Heidelberg, 2023).
- [22] H. Kleinert, *Gauge Fields in Condensed Matter*, Gauge Fields in Condensed Matter No. v. 2 (World Scientific, 1989).
- [23] M. Baggioli, M. Landry, and A. Zaccone, *Phys. Rev. E* **105**, 024602 (2022).
- [24] Z. W. Wu, Y. Chen, W.-H. Wang, W. Kob, and L. Xu, *Nature Communications* **14**, 2955 (2023).
- [25] M. Baggioli, *Nature Communications* **14**, 2956 (2023).
- [26] D. Şopu, A. Stukowski, M. Stoica, and S. Scudino, *Phys. Rev. Lett.* **119**, 195503 (2017).
- [27] D. Söpu, *Journal of Alloys and Compounds* **960**, 170585 (2023).
- [28] P. Desmarchelier, S. Fajardo, and M. L. Falk, “Topological characterization of rearrangements in amorphous solids,” (2024), [arXiv:2401.07109 \[cond-mat.mes-hall\]](https://arxiv.org/abs/2401.07109).
- [29] K. Kremer and G. S. Grest, *Phys. Rev. A* **33**, 3628 (1986).
- [30] K. Pearson and F. Galton, *Proceedings of the Royal Society of London* **58**, 240 (1895).
- [31] R. Dasgupta, H. G. E. Hentschel, and I. Procaccia, *Phys. Rev. Lett.* **109**, 255502 (2012).
- [32] V. Hieronymus-Schmidt, H. Rösner, G. Wilde, and A. Zaccone, *Phys. Rev. B* **95**, 134111 (2017).
- [33] M. Moshe, I. Levin, H. Aharoni, R. Kupferman, and E. Sharon, *Proceedings of the National Academy of Sciences* **112**, 10873 (2015).
- [34] N. S. Livne, A. Schiller, and M. Moshe, *Phys. Rev. E* **107**, 055004 (2023).
- [35] A. Kumar and I. Procaccia, *Europhysics Letters* (2023).
- [36] Y. Jin, I. Procaccia, and T. Samanta, *Physical Review E* **109**, 014902 (2024).
- [37] A. Zippelius, B. I. Halperin, and D. R. Nelson, *Phys. Rev. B* **22**, 2514 (1980).
- [38] M. J. Demkowicz and A. S. Argon, *Phys. Rev. B* **72**, 245205 (2005).
- [39] I. Kriuchevskiy, T. W. Sirk, and A. Zaccone, *Phys. Rev. E* **105**, 055004 (2022).
- [40] N. Oyama, H. Mizuno, and A. Ikeda, *Phys. Rev. Lett.* **127**, 108003 (2021).
- [41] J. N. Nampoothiri, Y. Wang, K. Ramola, J. Zhang, S. Bhattacharjee, and B. Chakraborty, *Phys. Rev. Lett.* **125**, 118002 (2020).
- [42] J. N. Nampoothiri, M. D’Eon, K. Ramola, B. Chakraborty, and S. Bhattacharjee, *Phys. Rev. E* **106**, 065004 (2022).
- [43] A. C. Y. Liu, E. D. Bojesen, R. F. Tabor, S. T. Mudie, A. Zaccone, P. Harrowell, and T. C. Petersen, *Science Advances* **8**, eabn0681 (2022).
- [44] A. Martinelli, F. Caporaletti, F. Dallari, M. Sprung, F. Westemeier, G. Baldi, and G. Monaco, *Phys. Rev. X* **13**, 041031 (2023).
- [45] S. Plimpton, *J. Comp. Phys* **117**, 1 (1995), see also: <http://lammps.sandia.gov>.